Inorganic Chemistry Communications 155 (2023) 111001

Contents lists available at ScienceDirect

Inorganic Chemistry Communications

journal homepage: www.elsevier.com/locate/inoche

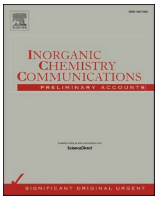

Short communication

Visible light-driven degradation of ofloxacin by graphene oxide-supported titania/zirconia ternary nanocomposites

Peiren Ding [a,1], Jiayi Li [a,1], Ming Guo [a], Haodong Ji [b,*], Peishen Li [c], Wen Liu [c,*], John Tressel [d], Shuai Gao [a], Qiang Wang [a,*], Shaowei Chen [d,*]

[a] Laboratory for Micro-sized Functional Materials & College of Elementary Education and Department of Chemistry, Capital Normal University, Beijing 100048, PR China
[b] School of Environment and Energy, Peking University Shenzhen Graduate School, Shenzhen, Guangdong 518055, PR China
[c] Beijing Innovation Center for Engineering Science and Advanced Technology (BIC-ESAT) and Key Laboratory of Water and Sediment Sciences, Ministry of Education, College of Environmental Sciences and Engineering, Peking University, Beijing 100871, PR China
[d] Department of Chemistry and Biochemistry, University of California, 1156 High Street, Santa Cruz, CA 95064, United States

ARTICLE INFO

Keywords:
Ofloxacin
TiO_2/ZrO_2/rGO ternary composite
Visible light
Heterojunction
Photocatalytic degradation

ABSTRACT

Ternary nanocomposites based on titanium dioxide (TiO_2) and zirconium dioxide (ZrO_2) supported on reduced graphene oxide (rGO) are prepared via a facile hydrothermal method and exhibit a markedly enhanced photocatalytic activity towards the degradation of ofloxacin under visible light irradiation, as compared to the individual components. Among the series, the sample prepared at the Ti:Zr atomic ratio of 9:1 exhibits the highest degradation efficiency of 94.6% under the irradiation of a 300 W xenon lamp, with a mineralization rate over 40%, and the performance remains virtually unchanged after 5 consecutive cycles of testing. Structural characterizations show that the formation of type I heterojunctions at the TiO_2/ZrO_2 and rGO interfaces enhances the interfacial charge transfer, and two possible degradation pathways are identified by results from density functional theory calculations, in conjunction with liquid chromatography-mass spectrometry analysis of the degradation intermediates. The photocatalytic degradation of ofloxacin is predicted to be efficient and environmentally friendly based on the Toxicity Estimation Software Tool (TEST) and quantitative structure–activity relationship (QSAR) analysis. These results underline the significant potential of TiO_2/ZrO_2/rGO ternary composites in the effective removal of toxic pollutants and wastewater treatment.

Antibiotics have been used widely on the global scale, and studies have shown that between 70% and 90% of antibiotics are excreted from the organisms into the environment either in their original forms or as toxic metabolites [1–4]. The accumulation of these compounds poses significant adversary effects on the environment and human health, as microorganisms that are drug-resistant can disrupt the ecological balance during material circulation and energy flow [5,6]. For instance, through the food chain, quinolone antibiotics can accumulate in the water systems and eventually enrich in the human body. Notably, among the water environments where antibiotics have been commonly detected are hospitals (35 μg/L), wastewater treatment plants (0.89–31.7 μg/L), and surface water (0.5 μg/L) [7,8].

Ofloxacin (OFL) is a common antibiotic for bacterial infection, where the strong C-F bonds render the compound chemically stable [9,10]. With the high electronegativity of F (3.98), OFL may adsorb onto a substrate surface via cation exchange, and the F sites can serve as a weak hydrogen bond acceptor for hydroxyl (–OH) groups [11]. These unique characteristics may impact the distribution of OFL in the environment, as well as its absorption, metabolism, and excretion of the body. Thus, development of effective technologies to eliminate OFL in wastewater is of both fundamental and technological significance. Conventionally, this is achieved by biodegradation [12], adsorption [13], chlorination [14], and others [15]. Yet, the nonbiodegradable and stable chemical structure of OFL makes conventional wastewater treatment methods unfeasible [16], and photocatalytic degradation has emerged as a viable strategy, in particular, under visible light irradiation [17–22].

Titanium dioxide (TiO_2) exhibits high photocatalytic efficacy under UV irradiation. Yet, the photocatalytic performance is rather limited in

---

[*] Corresponding authors.
E-mail addresses: jihaodong@pku.edu.cn (H. Ji), wen.liu@pku.edu.cn (W. Liu), qwchem@gmail.com (Q. Wang), shaowei@ucsc.edu (S. Chen).
[1] These authors contributed equally to this work.

https://doi.org/10.1016/j.inoche.2023.111001
Received 24 April 2023; Received in revised form 27 May 2023; Accepted 28 June 2023

the visible range, because of its wide band gap [23,24]. Similarly, zirconium dioxide (ZrO_2) has been widely used thanks to its high physicochemical stability and outstanding electronic band structure. However, the wide band gap (>5 eV) significantly limits the photocatalytic activity [25,26]. Nevertheless, when these two materials are combined into a composite, the formation of structural heterojunctions can markedly enhance the photocatalytic performance. Further enhancement can be achieved by the integration of a semiconducting material with a narrow bandgap, which facilitates the separation of photogenerated carriers. Within this context, graphene derivatives are viable candidates, in particular, graphene oxide (GO) and reduced graphene oxide (rGO) [27–29]. For example, Wang and coworkers [30] prepared TiO_2-rGO nanocomposites and observed that the strong electronic coupling at the TiO_2/rGO interface boosted the photocatalytic performance of phenol degradation in water. Oppong's group used a sol–gel method to prepare Gd-TiO_2-GO nanocomposites and observed a photocatalytic activity in the visible range [31]. In another study, GO/TiO_2 composites were obtained via the sol–gel route and used for the mineralization of primidone in aqueous solution under ozone and visible photoirradiation [32].

Herein, ternary composites of TiO_2/ZrO_2/rGO (TZGO) were prepared and showed an excellent photocatalytic performance towards the degradation of OFL under visible photoirradiation, due to effective charge transfer arising from the formation of type I heterojunctions between TiO_2/ZrO_2 and rGO. Seven samples were prepared hydrothermally at different Ti:Zr molar feed ratios, 1:0, 9:1, 7:3, 5:5, 3:7, 1:9, and 0:1, and referred to as TGO, TZGO-1, TZGO-2, TZGO-3, TZGO-4, TZGO-5, and ZGO, respectively (Table S1 in Supporting Information). The

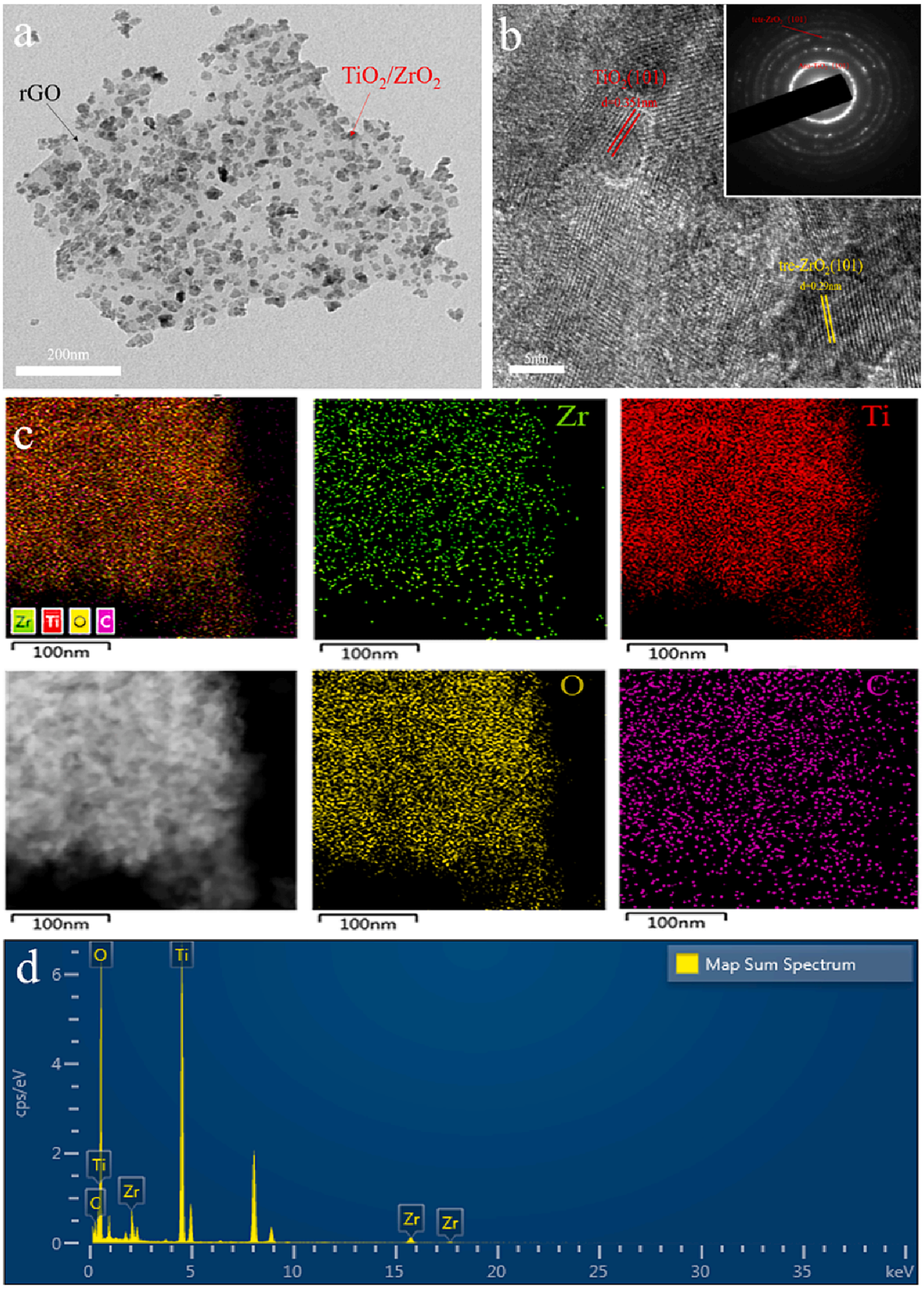

Fig. 1. (a,b) TEM images of the TZGO-1 nanocomposite. Inset to (b) is the SAED patterns. Scale bars are (a) 200 nm and (b) 5 nm. (c) Elemental maps of Zr, Ti, O and C, and (d) EDS spectrum of the TZGO-1 nanocomposite.

experimental details are included in the Supporting Information. X-ray diffraction (XRD) measurements were first carried out to characterize the structures of the obtained samples. From the XRD patterns (Fig. S1a in Supporting Information), the diffraction peaks at $2\theta = 25.4°$, $38.1°$, $48.2°$, $54.0°$, $55.2°$, and $62.7°$ can be ascribed to the (1 0 1), (0 0 4), (2 0 0), (1 0 5), (2 1 1), and (2 0 4) facets of anatase TiO_2 (JCPDS No. 21–1272) [33], whereas monoclinic ZrO_2 (JCPDS No. 86–1451), as well as a tetragonal phase of ZrO_2 (JCPDS No. 50–1089) can be found at $2\theta =$ 28.52° (1 1 1), 30.36° (1 0 1), 31.55° (1 0 5), 35.53° (1 1 0), 50.00° (2 0 0), and 59.96° (2 2 0) [34,35]. One can see that the anatase TiO_2 diffraction peaks became progressively weakened, while the diffraction peaks of monoclinic and tetragonal ZrO_2 gradually increased in intensity, as the Ti:Zr feed ratios decreased (that is, from TCN to TZCN and ZCN) [36].

In FTIR measurements (Fig. S1b in Supporting Information), it can be noted that all composites exhibited the vibrational characteristics of various functional moieties, O–H (3000—–3500 cm^{-1}, region v) [37], carboxylate or ketone C = O (1734 cm^{-1}, region iv), C–O–C (1227 cm^{-1}) and C–O (1055 cm^{-1}) (region iii) [38,39], and Zr–O (780 cm-1, region ii) [40]. Note that the Zr-O stretching vibration became intensified as the zirconium concentrations increased. The Ti-O-Ti vibrations in TZGO ternary composites also generated a series of vibrational bands between 400 and 700 cm^{-1} (region i) [41,42]. This is in good accord with data of the individual components of TiO_2, ZrO_2 and rGO.

The porosity of the nanocomposites was then examined by nitrogen sorption measurements. From Fig. S1c-d in Supporting Information, the samples can be observed to display a type IV isotherm with a H_3 hysteresis loop and pore size in the range of 1 to 50 nm, suggestive of the formation of abundant mesopores. The corresponding specific surface areas, pore sizes, and pore volumes are summarized in Table S2 in Supporting Information. One can see that TZGO-1 possessed a specific surface area of 169.99 m^2/g, pore size of 25.16 nm, and pore volume of 0.3275 cm^3/g, all the largest among the series.

In transmission electron microscopy (TEM) measurements (Fig. 1a), it can be clearly seen that TZGO-1 consisted of numerous TiO_2/ZrO_2 nanoparticles deposited on the surface of rGO nanosheets, and the nanoparticles exhibited clearly defined lattice fringes (Fig. 1b), featuring two interplanar distances, 0.35 and 0.29 nm, that can be ascribed to the (1 0 1) crystal planes of anatase TiO_2 and (1 0 1) crystal planes of tetragonal ZrO_2, respectively [43,44]. The selected area electron diffraction (SAED) patterns are depicted in the inset to Fig. 1b, where the TiO_2 (1 0 1) and ZrO_2 (1 0 1) rings can be readily identified. Additionally, from these TEM images, the formation of heterojunctions between TiO_2 and ZrO_2 as well as between TiO_2/ZrO_2 and rGO can be easily seen. From the elemental maps based on energy-dispersive X-ray spectroscopy (EDS) measurements, one can see that the C, O, Ti, and Zr elements were all distributed uniformly across TZGO-1, with a Ti/Zr atomic ratio of ca. 9:1, in agreement with the initial feed ratio (Fig. 1c-d). Consistent results were obtained for other samples in the series (Fig. S2 in Supporting Information).

The elemental composition and valency of the nanocomposites were then examined by X-ray photoelectron spectroscopy (XPS) measurements. From the survey spectra in Fig. S3a in Supporting Information), the C 1 s, O 1 s, Ti 2p, and Zr 2p electrons can be identified at 285.3, 530.2, 459.0, and 180.8 eV, respectively. The high-resolution scan of the Ti 2p electrons of TZGO-1 (Fig. S3b in Supporting Information) entailed a doublet at 464.7/458.6 eV, corresponding to the Ti $2p_{3/2}/2p_{1/2}$ electrons of TiO_2 [45]. In the Zr 4d scan (Fig. S3c in Supporting Information), one doublet was resolved at 182.3/184.3 eV, due to the Zr $3d_{3/2}/3d_{5/2}$ electrons of ZrO_2 [46]. Three peaks were deconvoluted from the high-resolution O 1 s spectrum (Fig. S3d in Supporting Information), due to the Ti-O-Ti at 531. 4 eV, Ti-OH at 532. 2 eV [42,47], and C-OH and/or C-O-C at 533.2 eV [48]. From the high-resolution C 1 s scan (Fig. S3e in Supporting Information), four species can be resolved, sp^2 hybridized C (284.6 eV), C-O (285.2 eV), C–C (286.3 eV), and Ti-O-C (288.3 eV) [49,50].

In electrochemical impedance spectroscopy (EIS) measurements [51], TZGO-1 exhibited the smallest arc diameter (i.e., charge transfer resistance, R_{CT}, Fig. 2b inset) in the Nyquist plot (Fig. 2a-b), suggesting the fastest electron-transfer kinetics among the sample series. Consistently, in transient photocurrent measurements (Fig. 2c) [52], the TZGO nanocomposites all exhibited a marked increment of the voltametric current upon visible photoirradiation using a xenon lamp as the light source, and TZGO-1 displayed the highest photocurrent among the series, suggesting most efficient separation of the photogenerated electron-hole pairs.

The band structure and interfacial charge transfer of TZGO were then examined by UV–vis diffuse reflectance spectroscopy (DRS) measurements. From Fig. 2d, all samples can be seen to exhibit an absorption threshold of ca. 400 nm, except for TZGO-4 and ZGO where the threshold was at a higher energy (about 300 nm) for the former and even higher at ca. 250 nm for the latter, in good agreement with the markedly higher bandgap of ZrO_2 as compared to that of TiO_2 [53]. In fact, from the Tauc plot (Fig. S4 in Supporting Information), TiO_2 can be seen to exhibit a forbidden band gap of 2.93 eV, in comparison to 4.63 eV for ZrO_2 [54,55 25,26].

The disparity of the electron-hole separation efficiency in the TZGO samples was further validated in steady-state and time-resolved photoluminescence measurements [56,57]. It can be seen from Fig. 2e that at the excitation wavelength of 390 nm, all samples in the series exhibited an emission peak at 410 nm, and TZGO-1 displayed the lowest emission intensity, suggesting least efficient recombination (and highest separation efficiency) of the photogenerated carriers [58]. These results were consistent with those obtained in time-resolved photoluminescence measurements at 390 nm excitation, where TZCN-1 exhibited the slowest decay of the transient profile (Fig. 2f), with the longest (average) decay time constant (t_A) of 24.8 ns [59,60].

The photocatalytic degradation of OFL by TZGO was conducted at the optimized pH of 9 and catalyst concentration of 0.2 g/L (Fig. S5 in Supporting Information). From Fig. 3a, one can see that (i) OFL alone was stable, (ii) OFL could be efficiently degraded upon the addition of the TZGO nanocomposites, and (iii) the performance increased with increasing concentration of Ti in the nanocomposite. After irradiation with visible light for 60 min, the degradation rate of OFL was 82.93% for TGO, 94.6 % for TZGO-1, 85.5% for TZGO-2, 64.4% for TZGO-3, 22.3% for TZGO-4, 33.4% for TZGO-5, and 14.5% for ZGO. That is, TZGO-1 emerged as the best among the sample series, where the degradation rate constant (k) of 0.01226 min^{-1} was the highest by pseudo-first-order kinetic fitting of the degradation data (Fig. 3b).

Furthermore, to assess the level of photocatalytic mineralization of sulfanilamide, the concentration of total organic carbon in the suspension was measured and compared before the photoreaction (TOC_0) and after 60 min of visible light exposure (TOC_e). As shown in Figure S6, the TOC_e/TOC_0 ratio increased in the order of TZGO-1 (0.59) < TGO (0.66) < TZGO-2 (0.71) < TZGO-3 (0.75) < TZGO-4 (0.79) < TZGO-5 (0.85) < ZGO (0.91), indicating that OFL was effectively mineralized during the photocatalytic degradation process, and TZGO-1 stood out with the highest mineralization rate.

Interference substances, such as Cl^-, NO_3^-, HCO_3^-, and DOM (dissolved organic matters), are often present in urban water and may significantly impact the photocatalytic degradation of OFL (Fig. S7 in Supporting Information). The ion concentrations (4 factors) as well as the experimental independent variables (29 experiments, Table S4 in Supporting Information) were based on literature findings and concentrations of inorganic anions in various regions within the City of Beijing. Based on the polynomial equation (1), the response result can be described by the efficiency percentage and the dependent variable by the ion concentration (mg/L),

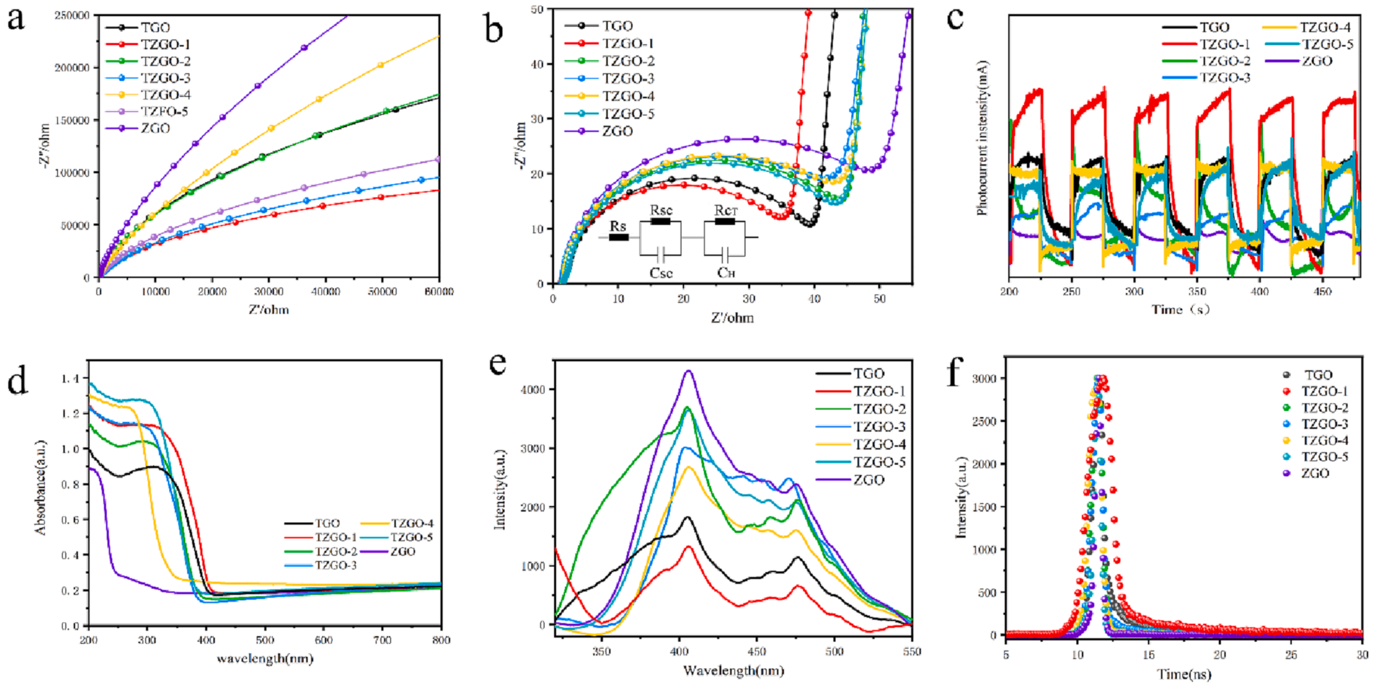

Fig. 2. (a, b) Nyquist plots. Inset to panel (b) is the equivalent circuit, where R_S is the series resistance (including the material resistance and contact resistance of the test system), R_{SC} is the charge-transfer resistance at the TZGO/electrode interface, and R_{CT} is the charge transfer resistance at the TZGO /electrolyte interface. C_{SC} is the capacitance of the TZGO/electrode interface (i.e., the internal capacitance of the material), and C_H is the capacitance of the TZGO/electrolyte interface. (c) Transient photocurrents and (d) UV–vis DRS spectra of the TZGO samples. (e) Steady-state and (f) time-resolved emission spectra of the TZGO samples at 390 nm excitation.

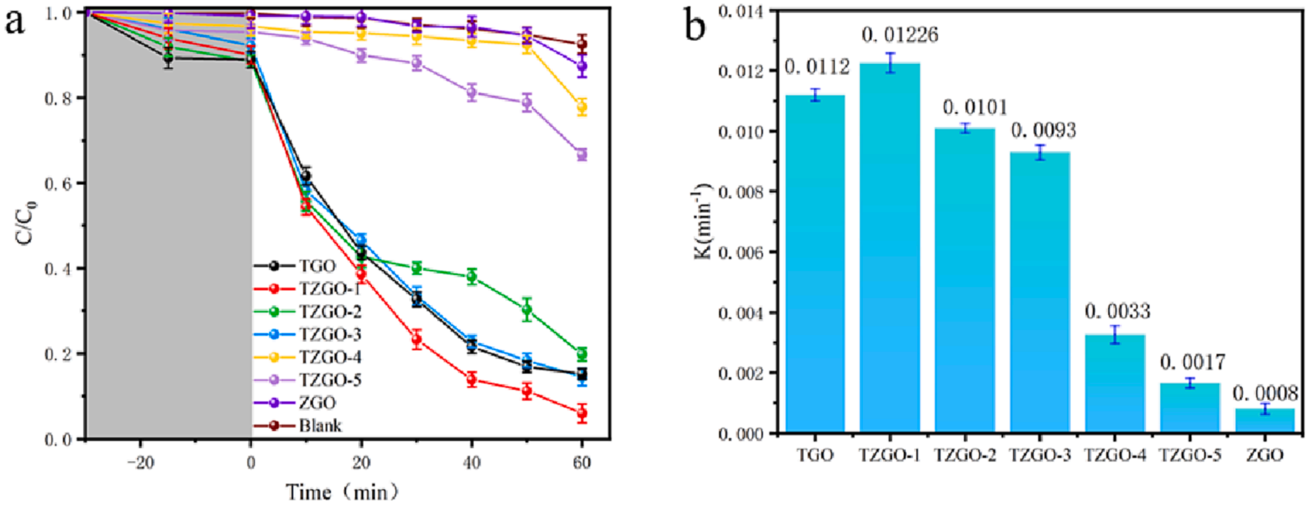

Fig. 3. (a) Photocatalytic degradation of OFL and (b) reaction rate constants of the sample series.

$$\begin{aligned} efficiency(\%) = {} & 73.14 + 0.014A - 0.57B + 2.7C + 0.038D + 7.2AB \\ & + 3.6AC - 0.69AD + 4.51BC - 1.73BD + 0.96CD - \\ & 1.36A^2 + 0.29B^2 + 2.17C^2 - 0.47D^2 \end{aligned} \tag{1}$$

The analysis of variance showed that the response findings from the simulated trials were in line with the predicted box-Behnken values (Table S5 in Supporting Information), with an estimated R^2 of 0.9875 and an adjusted R^2 of 0.9750. One can see that HCO_3^- has the highest influence on the photocatalytic performance, followed by NO_3^-, Cl^-, and DOM (Table S6 in Supporting Information), with the corresponding F value of 0.045, 8.63, 191.33, and 0.038 for the dependent variables, respectively. The three-dimensional response surface maps for each anion are shown in Fig. S7 in Supporting Information. Based on the Box-Behnken analysis, the most efficient conditions to eradicate OFL were identified at a Cl^- level of 78.00 mg/L, NO_3^- of 10.5 mg/L, DOM of 8.0 mg/L, and HCO_3^- of 100.00 mg/L. Note that inorganic anions have a detrimental impact on the photocatalytic removal of OFL by TZGO, as manifested by the simulated experiment results and Box-Behnken theoretical predictions. In practical applications, this may be mitigated by using a stronger photo illumination and/or a higher loading of photocatalysts [61].

Notably, upon the addition of p-benzoquinone (BQ), ammonium oxalate (AO), and isopropyl alcohol (IPA) into the reaction solution, which are the specific quenchers for hydroxyl radicals (•OH), holes (h^+), and superoxide anions ($O_2^{\bullet-}$) [60,62], respectively, the photodegradation of OFL exhibited a markedly different response. Specifically, virtually no impact on OFL degradation was noted with AO (Fig. S8a in Supporting Information), indicating minimal contribution of holes to the photocatalytic activity. By contrast, the addition of IPA and BQ led to a significant diminishment of the OFL degradation rate to only 61.13% and 21.61%, respectively, from over 90% in the absence of the radical quenchers, indicating that the photocatalytic degradation of OFL was primarily due to $O_2^{\bullet-}$ radicals, whereas •OH played only a minor role.

In electron paramagnetic resonance (EPR) measurements with 5,5-dimethyl-1-pyrroline-N-oxide (DMPO) as the trapping agent, superoxide and hydroxyl radicals were indeed detected [63,64]. It can see that the TZGO-1 sample displays only a featureless profile in the dark, and upon the irradiation with a xenon lamp (>420 nm), apparent spectral signals emerged within the magnetic field range of 3480 to 3560 G, which became increasingly intensified with prolonged illumination. In fact, both DMPO-$O_2^{\bullet-}$ (Fig. S8b in Supporting Information) and DMPO-•OH (Fig. S8c in Supporting Information) adducts can be identified. Note that the former was acquired in methanol, whereas the latter was obtained in water, due to the powerful reactivity of the •OH radicals with alcohols [65,66].

In XPS measurements (Fig. S8d in Supporting Information), the valence band maximum (VBM) positions were estimated to be 2.544 eV for TiO_2 and 3.501 eV for ZrO_2. Thus, in conjunction with the respective bandgap obtained from the Tauc plot (Fig. S4 in Supporting Information), the corresponding conduction band minimum (CBM) was −0.372 eV for TiO_2 and −1.131 eV for ZrO_2. As $E_{NHE}/V = \Phi + VBM - 4.44$, where Φ is the work function (3.88 V) and E_{NHE} is the potential vs. the normal hydrogen electrode (NHE), the CBM and VBM can be identified at −0.932 and + 1.994 V for TiO_2, and −1.691 V and + 2.941 V for ZrO_2. Upon photoirradiation, the formation of a type I heterojunction facilitated the transfer of h^+ in the VB and e^- in the CB of ZrO_2 to the VB and CB of TiO_2, respectively; and since rGO acts as a good conductor, the lifetime of photocarriers can be effectively improved. One should note that the VB potential of TiO_2 (+1.994 V) was significantly lower than the formal potential of H_2O/•OH (+2.72 V) [64,67], indicating that •OH radicals cannot be directly generated from water oxidation by h^+ of TiO_2. Yet, as the TiO_2 CB (-0.932 V) is drastically more negative, as compared to that of $O_2/\bullet O_2^-$ (-0.33 V), $O_2^{\bullet-}$ could be readily obtained by reduction of dissolved oxygen (O_2), then converted into HO_2^- and further into •OH, as detected in EPR measurements [68–71].

In the TZGO nanocomposites, charge transfer and hence photocatalytic production of radicals can be facilitated by the formation of type I heterojunctions between titania/zirconia and rGO (Fig. 4) [63,72–74]. Notably, the hole flow from the ZrO_2 VB to TiO_2 VB entails a smaller energy difference than the reverse migration of photogenerated electrons on the conduction bands. Therefore, the holes on TiO_2 VB most likely participate in the oxidation of water or oxygen adsorbed on the oxide surface to HO_2^- and eventually to •OH, which then degrades OFL in water. Note that the surface modification of ZrO_2 nanoparticles with TiO_2 and hence the formation of heterojunctions can also effectively reduce the grain boundary resistance and boost carrier conduction, which can be further enhanced by rGO, leading to a high quantum efficiency [75].

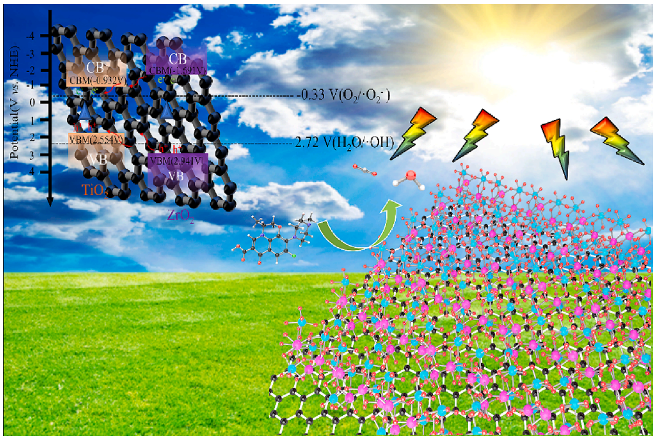

Fig. 4. Plausible mechanism of photodegradation of OFL by the TZGO ternary composites.

To unravel OFL degradation pathways and reaction mechanisms, the Fukui indices ($f^{0'}$) of the atomic sites in the molecular structure were evaluated by density functional theory (DFT) calculations (Fig. 5a). Note that the oxidative and reductive properties of organics depend on their highest occupied molecular orbitals (HOMO) and lowest unoccupied molecular orbitals (LUMO) [76]. As shown in Fig. 5b-c, when the phenyl ring is functionalized with F, the HOMO is situated mainly in the piperazine rings, a major site for electron loss and oxidative attack by h^+; meanwhile, LUMO is situated at the junctions of the tetrahydropyridine ring, benzene ring and carboxylic acid ring, which are the sensitive sites for electrophilic attack. Experimentally, upon photoirradiation of TZGO, oxygen radicals are generated and attack the HOMO and LUMO of OFL by subtracting electrons from HOMO and donating electrons to LUMO, producing cationic and anionic species, respectively. These species may then propagate and react with molecules in the surrounding environment, leading to OFL degradation. It should be noted that steric hindrance can play a significant role in determining the effectiveness of the free radical attack, as the bulky side groups in the molecule can hinder the access of free radicals to the reactive sites. Fig. 5d shows the molecular structure and Fukui indices of the various atomic sites of OFL. Note that although the $f^{0'}$s of C8 (0.0815) and C1 (0.0467) on the piperazine ring are lower than that of N29 (0.0944), they are unlikely to be the $\cdot O_2^-/\cdot OH$ attack sites due to steric hindrance [77,78].

Liquid chromatography-mass spectrometry (LC-MS) measurements were then performed to identify the OFL degradation intermediates, which entailed two distinct OFL degradation routes (Fig. 5e, and Fig. S9 in Supporting Information). In pathway I, the aromatic ring of OFL was oxidatively opened, and attack of the N29 site by active radicals led to the breaking of the C-N bond and the production of C ($m/z = 127$) and D ($m/z = 86$) intermediates. In addition, the Fukui index of the C1 site suggests ready cleavage of the C–C bond. In pathway II, the C–C link bridging the carboxyl group and the phenyl ring was broken to produce B ($m/z = 288$), and the C–C bond connecting the piperazine ring and the benzene ring at C5 was broken to produce G ($m/z = 269$). Lastly, the cleavage between the piperazine and benzene rings produced intermediate I ($m/z = 269$), as did the reaction between the carboxyl group and the benzene ring. O13 has a higher Fukui index, and the C-O bond in C was broken to produce J ($m/z = 269$), as a result of the attack by reactive free radicals. After prolonged reaction with free radicals, the OFL intermediates were mineralized into harmless compounds, like CO_2 and H_2O [79–81].

Toxicity of the reaction intermediates produced during OFL degradation was then analyzed by using the Toxicity Estimation Software Tool (TEST) and quantitative structure–activity relationship (QSAR) methods, where the lethal doses (LD_{50}), mutagenicity, and developmental toxicity were analyzed and compared of the OFL and by-products A-J generated during the photodegradation process [82,83]. We can determine that 1882.40 mg/kg of OFL is a "toxic" dose (Fig. S10a in Supporting Information). Three intermediates (A, B, and G) were produced after further degradation; and all three were more hazardous than OFL, with an LD_{50} reaching the "extremely toxic" level for both A and B. However, the toxicity was greatly reduced, once the benzene and pyridine rings were cleaved, with D of 1902.51 mg/kg and J of 1490.50 mg/kg, respectively, compared to OFL.

Additionally, the first degradation products of OFL by TZGO, A and B, have a lower developmental toxicity than OFL itself, with only G being more toxic (Fig. S10b in Supporting Information). The

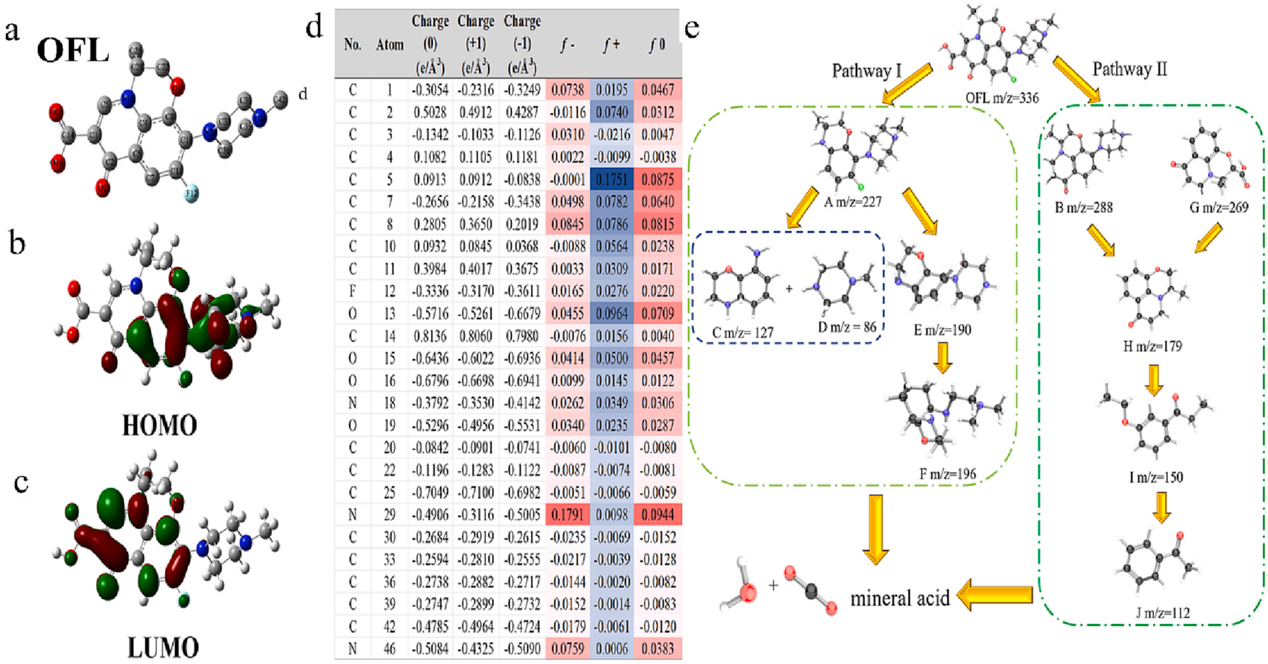

No.	Atom	Charge (0) (e/Å^3)	Charge (+1) (e/Å^3)	Charge (-1) (e/Å^3)	f -	f +	f 0
C	1	-0.3054	-0.2316	-0.3249	0.0738	0.0195	0.0467
C	2	0.5028	0.4912	0.4287	-0.0116	0.0740	0.0312
C	3	-0.1342	-0.1033	-0.1126	0.0310	-0.0216	0.0047
C	4	0.1082	0.1105	0.1181	0.0022	-0.0099	-0.0038
C	5	0.0913	0.0912	-0.0838	-0.0001	0.1751	0.0875
C	7	-0.2656	-0.2158	-0.3438	0.0498	0.0782	0.0640
C	8	0.2805	0.3650	0.2019	0.0845	0.0786	0.0815
C	10	0.0932	0.0845	0.0368	-0.0088	0.0564	0.0238
C	11	0.3984	0.4017	0.3675	0.0033	0.0309	0.0171
F	12	-0.3336	-0.3170	-0.3611	0.0165	0.0276	0.0220
O	13	-0.5716	-0.5261	-0.6679	0.0455	0.0964	0.0709
C	14	0.8136	0.8060	0.7980	-0.0076	0.0156	0.0040
O	15	-0.6436	-0.6022	-0.6936	0.0414	0.0500	0.0457
O	16	-0.6796	-0.6698	-0.6941	0.0099	0.0145	0.0122
N	18	-0.3792	-0.3530	-0.4142	0.0262	0.0349	0.0306
O	19	-0.5296	-0.4956	-0.5531	0.0340	0.0235	0.0287
C	20	-0.0842	-0.0901	-0.0741	-0.0060	-0.0101	-0.0080
C	22	-0.1196	-0.1283	-0.1122	-0.0087	-0.0074	-0.0081
C	25	-0.7049	-0.7100	-0.6982	-0.0051	-0.0066	-0.0059
N	29	-0.4906	-0.3116	-0.5005	0.1791	0.0098	0.0944
C	30	-0.2684	-0.2919	-0.2615	-0.0235	-0.0069	-0.0152
C	33	-0.2594	-0.2810	-0.2555	-0.0217	-0.0039	-0.0128
C	36	-0.2738	-0.2882	-0.2717	-0.0144	-0.0020	-0.0082
C	39	-0.2747	-0.2899	-0.2732	-0.0152	-0.0014	-0.0083
C	42	-0.4785	-0.4964	-0.4724	-0.0179	-0.0061	-0.0120
N	46	-0.5084	-0.4325	-0.5090	0.0759	0.0006	0.0383

Fig. 5. (a) OFL chemical structure. (b) HOMO and (c) LOMO isodensity distributions of OFL. (d) Condensed Fukui index (f^0) of OFL. (e) Analysis of possible intermediates and degradation pathways of OFL.

intermediates C, D, and F of degradation pathway I and intermediate J of pathway II will eventually become non-developmentally toxic. Photocatalytic removal of OFL by TZGO at the initial stage produces intermediates A, B, and G that are more mutagenic than OFL itself (Fig. S10c in Supporting Information), and as the degradation of OFL progresses, most of the intermediates in pathways I and II showed negative mutagenicity levels (<0.5).

That is, TZGO may produce intermediates in the process of degrading OFL that are more toxic than OFL itself, but as the photocatalytic reaction progresses, these intermediates will become less toxic, and decompose further into less toxic or even nontoxic products. The results of this study demonstrate that TZGO can be used as an effective and clean catalyst not only for removing OFL but also for preventing secondary pollution.

TZGO-1 can be recycled and reused for multiple times. Under similar conditions, the degradation efficiency after five consecutive photocatalytic experiments was reduced only by 4%, attesting the excellent durability of TZGO-1 (Fig. S11a in Supporting Information). Consistent results were obtained in cyclic voltammetry measurements (Fig. S11b in Supporting Information).

In conclusion, TZGO ternary nanocomposites were synthesized hydrothermally, where TiO_2/ZrO_2 nanoparticles were deposited onto rGO nanosheets. In comparison to relevant catalysts in the literature (Table S7), the TZGO composites leveraged the high electrical conductivity of rGO and the formation of type I heterojunctions that impeded the recombination of photogenerated carriers. Under visible photoirradiation, TZGO-1 exhibited the highest efficiency towards OFL degradation at 94.63% in one hour, among the series. In five consecutive cycles of photocatalytic testing, the photodegradation efficiency remained over 90%, indicating outstanding structural stability of the TZGO composites. The remarkable performance was attributed to the enhanced separation of photogenerated carriers in TiO_2/ZrO_2, which facilitated the effective production of $O_2^{\bullet -}$ and •OH radicals. Quenching experiments with select radical scavengers confirmed that $O_2^{\bullet -}$ radicals were the predominant contributor, with •OH being the minor one. LC-MS analysis, in combination with DFT calculations, showed that the OFL degradation likely involved two major pathways, and the toxicity of all OFL degradation intermediates was analyzed using QSAR analysis. Most intermediates were less toxic than OFL, and the breakdown process would not cause any subsequent environmental damage. Results from this study provide a practical and eco-friendly strategy for the rational design and engineering TiO_2/ZrO_2/rGO ternary nanocomposites as high-performance photocatalysts.

Declaration of Competing Interest

The authors declare that they have no known competing financial interests or personal relationships that could have appeared to influence the work reported in this paper.

Data availability

Data will be made available on request.

Acknowledgment

This work was supported by the Natural Science Foundation of China (NSFC, 21471103 and 52100069). S.W.C. thanks the National Science Foundation for partial support of the work (CBET-1848841 and CHE-2003685).

Appendix A. Supplementary material

Supplementary data to this article can be found online at https://doi.org/10.1016/j.inoche.2023.111001.

References

[1] S. Li, C. Wang, Y. Liu, et al., Chem. Eng. J. 415 (2021).
[2] Y. Wang, D. Yu, W. Wang, et al., Sep. Purif. Technol. 239 (2020).
[3] W. Wang, R. Yang, T. Li, et al., Compos. Part B-Eng. 205 (2021).
[4] A. Sadeghzadeh-Attar, J. Taiwan. Inst. Chem. E. 111 (2020) 325–336.
[5] P.M. Clyde, C.S. Lee, R.E. Price, et al., Water. Res. 206 (2021), 117743.
[6] X. Shi, B. Ren, X. Jin, et al., J. Hazard. Mater. 432 (2022), 128539.
[7] J. Radjenovic, M. Petrovic, D. Barcelo, Water. Res. 43 (2009) 831–841.
[8] R. Yang, S. Zhong, L. Zhang, et al., Sep. Purif. Technol. 235 (2020).
[9] E. Gullberg, S. Cao, O.G. Berg, et al., PLoS. Pathog. 7 (2011) e1002158.
[10] T. Li, S. Lu, W. Lin, et al., Chem. Eng. J. 433 (2022).

[11] J.E.N. Swallow, B.A.D. Williamson, T.J. Whittles, et al., Adv. Funct. Mater. 28 (2018).
[12] S.M. Emadian, T.T. Onay, B. Demirel, Waste. Manag. 59 (2017) 526–536.
[13] L. Ruiping, L. Chunye, L. Xitao, RSC Advances 6 (2016) 19872–19877.
[14] X. Xu, D. Wang, C. Li, et al., Environ. Pollut. 225 (2017) 412–418.
[15] A. Fakhru'l-Razi, A. Pendashteh, L.C. Abdullah, et al., J. Hazard. Mater. 170 (2009) 530–551.
[16] J. Wang, L. Chu, L. Wojnarovits, et al., Sci. Total. Environ. 744 (2020), 140997.
[17] X.-J. Wen, C.-G. Niu, L. Zhang, et al., J. Catal. 358 (2018) 141–154.
[18] Y. Hong, C. Li, G. Zhang, et al., Chem Eng J. 299 (2016) 74–84.
[19] Z. Cai, A.D. Dwivedi, W.-N. Lee, et al., Environ. Science Nano. 5 (2018) 27–47.
[20] P. Ding, H. Ji, P. Li, et al., Appl. Catal. B: Environ. (2021), 120633.
[21] R. Yang, F. Dong, X. You, et al., Mater. Lett. 252 (2019) 272–276.
[22] H. Zhang, D. Yu, W. Wang, et al., Appl. Surf. Sci. 497 (2019).
[23] Q. Guo, Z. Ma, C. Zhou, et al., Chem. Rev. 119 (2019) 11020–11041.
[24] H. Hussain, G. Tocci, T. Woolcot, et al., Nat. Mater. 16 (2017) 461–466.
[25] B. Jin, H. Poelman, C. Detavernier, et al., Appl Catal B: Environ 292 (2021), 120194.
[26] B. Jin, S. Li, Y. Liu, et al., Chem. Eng. J. 436 (2022).
[27] H. Li, P. Wang, X. Yi, et al., Appl. Catal. B Environ. 264 (2020).
[28] Yang, R. Z., Z.; Hu, C., et al., Chem Eng J. 390 (2020) 124522.
[29] Y. Wang, K. Ding, R. Xu, et al., J. Clean. Prod. 247 (2020).
[30] P. Wang, J. Wang, X. Wang, et al., Appl. Catal. B: Environ. 132–133 (2013) 452–459.
[31] S.-O.-B. Oppong, F. Opoku, P.P. Govender, Appl. Catal. B: Environ. 243 (2019) 106–120.
[32] M. Checa, M. Figueredo, A. Aguinaco, et al., J. Hazard. Mater. 369 (2019) 70–78.
[33] S.W. Sweeney, G. Roseman, C.P. Deming, et al., Int. J. Hydrogen Energy 41 (2016) 18005–18014.
[34] A. Naldoni, M. Altomare, G. Zoppellaro, et al., ACS Catal 9 (2019) 345–364.
[35] K. Wu, M. Yang, W. Pu, et al., Acs Sustain Chem Eng 5 (2017) 3509–3516.
[36] E.N. Al-Shafei, D. Robert Brown, S.P. Katikaneni, et al., Chem. Eng. J. 419 (2021).
[37] M. Xu, L. Han, S. Dong, ACS Appl. Mater. Interfaces. 5 (2013) 12533–12540.
[38] Q. Li, B. Guo, J. Yu, et al., J Am Chem Soc 133 (2011) 10878–10884.
[39] M.J. Kang, C.W. Kim, H.G. Cha, et al., Appl. Catal. B: Environ. 295 (2021).
[40] J. Tian, Q. Shao, J. Zhao, et al., J. Colloid. Interf. Sci. 541 (2019) 18–29.
[41] Huang, Z. a.; Sun, Q.; Lv, K., et al., Appl. Catal. B: Environ. 164 (2015) 420-427.
[42] R. Hao, G. Wang, H. Tang, et al., Appl. Catal. B: Environ. 187 (2016) 47–58.
[43] Y. Wang, J. Liu, Y. Ozaki, et al., Angew. Chem. Int. Ed. Engl. 58 (2019) 8172–8176.
[44] D. Li, J. Yao, B. Liu, et al., Appl. Surf. Sci. 471 (2019) 394–402.
[45] S.H. Liu, W.X. Lin, J. Hazard. Mater. 368 (2019) 468–476.
[46] M. Huang, Y. Zhang, Y. Zhou, et al., New. J. Chem. 41 (2017) 13472–13482.
[47] J. Hu, H. Li, Q. Wu, et al., Chem. Eng. J. 263 (2015) 144–150.
[48] J. Tian, S. Liu, Y. Zhang, et al., Inorg. Chem. 51 (2012) 4742–4746.
[49] Y. Shiraishi, S. Shiota, H. Hirakawa, et al., ACS Catalysis 7 (2016) 293–300.
[50] Á. Tolosana-Moranchel, A. Manassero, M.L. Satuf, et al., Appl. Catal. B: Environ. 246 (2019) 1–11.
[51] G. Di, Z. Zhu, H. Zhang, et al., J. Colloid. Interface Sci. 538 (2019) 256–266.
[52] L. Wang, Z. Zhang, R. Guan, et al., Nano Res. 15 (2022) 8010–8018.
[53] T. Giannakopoulou, I. Papailias, N. Todorova, et al., Chem. Eng. J. 310 (2017) 571–580.
[54] X.H. Yi, S.Q. Ma, X.D. Du, et al., Chem. Eng. J. 375 (2019), 121944.
[55] Q. Han, B. Wang, J. Gao, et al., ACS Nano 10 (2016) 2745–2751.
[56] C. Ye, J.-X. Li, Z.-J. Li, et al., ACS Catal. 5 (2015) 6973–6979.
[57] H. Shi, G. Chen, C. Zhang, et al., ACS Catal. 4 (2014) 3637–3643.
[58] G. Zhang, T. Zhang, B. Li, et al., Appl. Sur. Sci. 433 (2018) 963–974.
[59] X. She, L. Liu, H. Ji, et al., Appl. Catal. B: Environ. 187 (2016) 144–153.
[60] J. Xu, Q. Gao, Z. Wang, et al., Appl. Catal. B: Environ. 291 (2021).
[61] X.H. Yi, H. Ji, C.C. Wang, et al., Appl. Catal. B: Environ. 293 (2021), 120229.
[62] X.M. Xu, L.J. Meng, J. Luo, et al., Appl Catal B-Environ 293 (2021).
[63] Z. Zhao, J. Bian, L. Zhao, et al., Chin. J. Catal. 43 (2022) 1331–1340.
[64] T. Lv, D. Li, Y. Hong, et al., Dalton. Trans. 46 (2017) 12675–12682.
[65] Y. Yang, G. Zeng, D. Huang, et al., Appl. Catal. B: Environ. 272 (2020).
[66] W. Li, L. Jin, F. Gao, et al., Appl. Catal. B: Environ. 294 (2021).
[67] H. Ji, P. Du, D. Zhao, et al., Appl. Catal. B: Environ. 263 (2020), 118357.
[68] Jo, W. K.; Clament Sagaya Selvam, N., J. Hazard. Mater. 299 (2015) 462-470.
[69] W.Y. Teoh, J.A. Scott, R. Amal, J. Phys. Chem. Lett. 3 (2012) 629–639.
[70] G. Chata, F. Nichols, R. Mercado, et al., ACS Appl Bio Mater. 4 (2021) 7025–7033.
[71] F. Nichols, K.I. Ozoemena, S.W. Chen, Chin. J. Catal. 43 (2022) 1399–1416.
[72] F.R. Pomilla, E.I. García-López, G. Marcì, et al., Mater Todat Sustain 13 (2021), 100071.
[73] J. Zhang, L. Li, Z. Xiao, et al., Acs. Appl. Mater. Inter. 4 (2016) 2037–2046.
[74] Y. Gao, J. Zhu, H. An, et al., J. Phys. Chem. Lett. 8 (2017) 1419–1423.
[75] S. Ramamoorthy, S. Das, R. Balan, et al., J. Alloy. Compd. 898 (2022).
[76] F. Wang, Y. Feng, P. Chen, et al., Appl. Catal. B: Environ. 227 (2018) 114–122.
[77] D. Zhang, J. Qi, H. Ji, et al., Chem. Eng. J. 400 (2020).
[78] Q. Su, J. Li, H. Yuan, et al., Chem. Eng. J. 427 (2022).
[79] Z. Du, K. Li, S. Zhou, et al., Chem. Eng. J. 380 (2020).
[80] G. Liu, Y. Zhang, H. Yu, et al., J. Hazard. Mater. 397 (2020), 122783.
[81] P. Chen, L. Blaney, G. Cagnetta, et al., Environ. Sci. Technol. 53 (2019) 1564–1575.
[82] L. Chen, H. Ji, J. Qi, et al., Chem. Eng. J. 406 (2021), 126877.
[83] H. Ji, W. Liu, F. Sun, et al., Chem. Eng. J. 419 (2021), 129605.